Population balance modelling of magnesium hydroxide precipitation: Full validation on different reactor configurations

Antonello Raponi [a],[*], Ramona Achermann [b], Salvatore Romano [c], Silvio Trespi [b], Marco Mazzotti [b], Andrea Cipollina [c], Antonio Buffo [a], Marco Vanni [a], Daniele Marchisio [a]

[a] *Politecnico di Torino, Institute of Chemical Engineering, Department of Applied Science and Technology, 10129 Torino, Italy*
[b] *Institute of Energy and Process Engineering, ETH Zurich, 8092 Zurich, Switzerland*
[c] *Dipartimento di Ingegneria, Università degli Studi di Palermo, viale delle Scienze Ed.6, 90128 Palermo, Italy*

ARTICLE INFO

ABSTRACT

In this paper, a predictive mono-dimensional (1D) model for $Mg(OH)_2$ precipitation is proposed and its predictive capability is tested. Two different reactor configurations are analyzed and compared, namely a T-mixer and a Y-mixer followed by two consecutive diverging channels and a final coil of constant diameter. Both setups were chosen for their high mixing efficiency. The suspension samples were characterized by Dynamic Light Scattering (DLS), thus obtaining particle size distributions (PSD). The experimental data collected using the T-mixer was used to identify the kinetics parameters set, while the data obtained through the Y-mixer setup was employed to assess the model predictive capability under different fluid dynamics conditions. Computational Fluid Dynamics (CFD) simulations were conducted to characterize the flow fields and the turbulence, which were integrated into the 1D model. Predictions were found to be in good agreement with the experimental data and further improved after introducing a novel correction factor for the aggregation kernel.

1. Introduction

The synthesis of magnesium hydroxide ($Mg(OH)_2$) particles has gained increasing attention in recent years due to its broad range of applications [1–7]. $Mg(OH)_2$ is typically produced via the hydro-thermal synthesis method [8]. However, this process is quite energy-intensive due to the high temperatures required. Thus, other synthesis routes have been explored and proposed [8–10]. One of them is the extraction of magnesium from brines and bitterns by reaction with an alkaline solution. As a result of the reaction, the solute concentration in the solution increases to the point where it exceeds its equilibrium solubility, generating supersaturation and leading to the subsequent precipitation of magnesium as $Mg(OH)_2$. Precipitation is a fast process that produces an insoluble crystalline substance [11]. It is generally characterized by very high levels of supersaturation, which result in a burst of primary nuclei and their subsequent growth. In addition to these molecular phenomena (i.e., primary nucleation and molecular growth), secondary processes can occur [12] such as agglomeration (weak physical bridges through the surrounding liquid), aggregation (strong chemical bridges due to supersaturation depletion), or ageing. Since some of these phenomena are very fast, mixing at all scales plays

a crucial role. Baldyga et al. [13], Marchisio et al. [14,15] and Marchisio and Barresi [16] demonstrated the key role of mixing. It influences supersaturation build-up, which affects nucleation, growth, and aggregation rates, determining the final morphology and size of the particles. A micro-mixing model is, therefore, necessary to properly describe the precipitation processes. Danckwerts [17], among the first, tried to model the effect of micro-mixing on fast reactions. In addition, Becker and Larson [18] computationally described the micro-segregation and micro-mixing in continuous crystallization processes. In recent years, due to the increase in computational power, some researchers have investigated mixing (and its efficiency) by exploiting different numerical approaches through three-dimensional Computational Fluid Dynamics (CFD) simulations. For instance, Schikarski et al. [19,20] quantified the mixing efficiency in a T-mixer through Direct Numerical Simulations (DNS) and validated the associated prediction with experimental data. Shiea et al. [21], instead, used a Reynolds-averaged Navier–Stokes equation approach (RANS) and a multi-environment model to account for micro-mixing [22]. However, also a computationally cheaper route can be taken. For example, (approximate) equations that directly incorporate information from hydrodynamic and mixing, empirically derived, can be used [23]. Some turbulent properties

---

* Corresponding author.
E-mail address: antonello.raponi@polito.it (A. Raponi).

(i.e., the turbulent kinetic energy, k, and the turbulent dissipation rate, ε) are of paramount importance in the description of micro-mixing. The higher the turbulence, the faster the mixing at the molecular scale. Moreover, turbulence strongly influences secondary processes, such as aggregation and agglomeration. Bałdyga and Orciuch [24], Wang et al. [25], Gavi et al. [26] have studied the hydrodynamics aspects affecting aggregation. They related the hydrodynamics to the collision rate stating that an increase in turbulence might lead to an increase in the collision frequency between particles. On the other hand, turbulence also affects the aggregation efficiency [27]. The aggregation efficiency is proportional to the local supersaturation of the system; the higher the supersaturation, the greater the likelihood that two colliding particles cement together. However, the aggregation efficiency also depends on the interaction time between the two colliding particles, which is inversely proportional to the turbulent shear stress. In other words, the higher the shear, the shorter the time that two particles can remain close enough to form a stable bridge. This relationship between aggregation efficiency and turbulent shear stress is related to the turbulent dissipation rate, ε. Therefore, the overall effect on the collision rate is not trivial, and it is represented in the model by the product of the aggregation kernel and the aggregation efficiency.

In this work, we account for the effect of turbulence on micro-mixing and aggregation by using a mono-dimensional uni-variate population balance model (PBM). Based on the RANS approach, CFD simulations are run to characterize the turbulence in the investigated reactors. Particular attention is paid to the turbulent kinetic energy, k, and the turbulent dissipation rate, ε, profiles. Their ratio determines the micro-mixing rate, and ε directly influences the collision rate. The PBM contains unknown kinetic parameters, accounting for the nucleation, molecular growth and aggregation rates, that are estimated by comparison with experimental data collected by using the T-mixer setup. The predictions from the PBM are then compared with experimental data collected by using a different reactor setup, namely a Y-mixer. Furthermore, a novel correction factor for the aggregation kernel is proposed here for the first time, allowing further improvements in the model predictive capability. This predictive model (and framework) will be used for the design and optimization of a crystallizer prototype.

The manuscript is structured as follows. Section 2 describes the $Mg(OH)_2$ precipitation experiments conducted in the T- and the Y-mixers, and the differences between the experimental data sets are explained. The mixing features of the two mixers are investigated (Section 3), and then, the PBM simulations are used to interpret the experimental results (Section 4). Finally, conclusions are drawn in Section 5.

2. Experimental methods and design

In this section, we compare data from two experimental setups: a T-mixer and a Y-mixer. The T-mixer setup and its results were discussed in our previous work [28] and briefly summarized hereafter. A circular-cross section T-mixer with a constant diameter of 2 mm and mixing channel length of 4 cm was employed. The Y-mixer setup, described by Orlewski and Mazzotti [29], consists of two arms with a diameter of 0.5 mm and a mixing channel diameter of 1 mm and a length of 3 mm. The angle between the two arms is 120°. Following the mixing channel, there are two consecutive diverging channels: the former of final diameter equal to 1.5 mm and a total length of 3.5 mm; the latter of final diameter equal to 4 mm and a total length equal to 5 mm. The setup ends with a constant diameter pipe. This fourth section was changed according to the reactant concentrations. For higher reactant concentrations (i.e., 0.125 up to 1 M), a shorter straight pipe of 40 cm was used, whereas for lower reactant concentrations (down to 0.01 M), a coil of a total length of 10 m was used to ensure the completion of the reaction. Details of the two explored geometries are given in the supplementary material. The reactants were fed to each arm using two

micro-gear pumps (mzr-11508X1, HNP Germany), assuring a pulsation-free flow. The setup was controlled using a LabView program. Two Coriolis mass flow meters (M15, Bronkhorst, The Netherlands) were used to send the set point signal to the pumps.

Magnesium chloride hexahydrate powder (>99.0%, Sigma-Aldrich) and Sodium Hydroxide pellets (>98.0%, Sigma-Aldrich, ACS reagent) were used to prepare the corresponding aqueous solutions at each concentration. The solutions were separately pumped through each arm and impinge in the mixing channel, where the precipitation of $Mg(OH)_2$ occurred.

In Table 1, the operating conditions for both the T- and Y-mixer are reported. The NaOH concentration obeys the stoichiometry of the reaction for all the operating conditions:

$$Mg^{2+}_{(aq)} + 2OH^-_{(aq)} \rightarrow Mg(OH)_{2(s)} \downarrow \tag{1}$$

A sample of the suspension exiting the mixing channel was collected, and the particle size distributions (PSD) were measured using the Dynamic Light Scattering (DLS; Zetasizer Nano ZS, Malvern Instruments, UK) technique. For this, the following procedure was followed: (i) the suspension was diluted, if necessary, to ensure that the same solid mass of 0.3 g/L per unit suspension volume was reached, (ii) an anti-agglomeration agent (poly-acrylic acid, sodium salt) was added (4.9 g/kg) to suppress agglomeration and, in the end, (iii) the sample was left in an ultrasound bath (Elmasonic S 40 (H), Singen, Germany) for 5 min. The protocol makes it possible not only to neglect agglomeration, but also to stabilize suspension by arresting possible changes in PSDs [28]. From the experimentally measured PSD, moments were calculated according to the following definition:

$$m_j = \int_0^\infty L^j f(L) \, dL \tag{2}$$

where L is the particle size and $f(L)$ is the PSD. Correspondingly, the moment ratios d_{ij} are defined as:

$$d_{ij} = \frac{m_i}{m_j} \tag{3}$$

Since these characteristic sizes (such as $d_{10}, d_{21}, d_{32}, d_{43}$) are calculated from integral properties (i.e., the moments of the PSD) tracing their evolution means tracing the evolution of the whole PSD. Therefore, although all characteristic sizes are monitored, we chose to focus the discussion only on d_{10} for the sake of discussion. This choice is also supported by the observation that the distributions that the DLS can provide are generally poorly polydisperse. It means, therefore, that the characteristic sizes always exhibit the same qualitative trend, and the absolute value of the dimensions increases as the monitored size increases (i.e., $d_{10} < d_{21} < d_{32} < d_{43}$) as reported in the 'supporting information'. Fig. 1 shows the number-averaged mean particle size extracted from the experiments conducted in the T- and Y-mixers for different initial $MgCl_2$ concentrations. One can see that similar values of d_{10} were obtained. In the case of the Y-mixer, the $MgCl_2$ concentrations range investigated initially was extended towards smaller concentration levels, and a minimum in d_{10} was observed. Experiments at lower concentrations in the T-mixer were also carried out and show good agreement with simulations. However, the results from these experiments are not reported in this study due to the presence of experimental uncertainty that is difficult to quantify. This uncertainty is primarily related to the impossibility of controlling where the end of the reaction occurs, particularly at low concentrations. In this scenario, there is a possibility of some unconsumed supersaturation remaining at the T-mixer outlet, which could lead to further particles evolution within the collection flask. While it is reasonable to assume that this variation is not significant, as the supersaturation at the outlet will have been consumed in large amounts and further gets diluted in the collection flask, it remains challenging to precisely estimate the uncertainty in particle sizes. In contrast, the Y-mixer experiments benefited from the possibility of guaranteeing adequate residence times by extending

Table 1
Operating conditions adopted for the T- and Y-mixer.

Geometry	Operative conditions					
	Concentration (M)	Residence time (ms)	Reynolds number	Flow rate (mL/min)	Estimate mixing time (ms)	Reactor length (cm)
T-Mixer	0.125	~ 3	$2.7 \cdot 10^4$	2320	2	4
	0.25	~ 3	$2.7 \cdot 10^4$	2320	2	4
	0.5	~ 3	$2.7 \cdot 10^4$	2320	2	4
	0.75	~ 3	$2.7 \cdot 10^4$	2320	2	4
	1	~ 3	$2.7 \cdot 10^4$	2320	2	4
Y-Mixer	0.01	$\sim 9 \cdot 10^3$	$1.7 \cdot 10^4$	835	0.6	10^3
	0.025	$\sim 9 \cdot 10^3$	$1.7 \cdot 10^4$	835	0.6	10^3
	0.05	$\sim 9 \cdot 10^3$	$1.7 \cdot 10^4$	835	0.6	10^3
	0.125	$\sim 3.6 \cdot 10^2$	$1.7 \cdot 10^4$	835	0.6	40
	0.5	$\sim 3.6 \cdot 10^2$	$1.7 \cdot 10^4$	835	0.6	40
	1	$\sim 3.6 \cdot 10^2$	$1.7 \cdot 10^4$	835	0.6	40
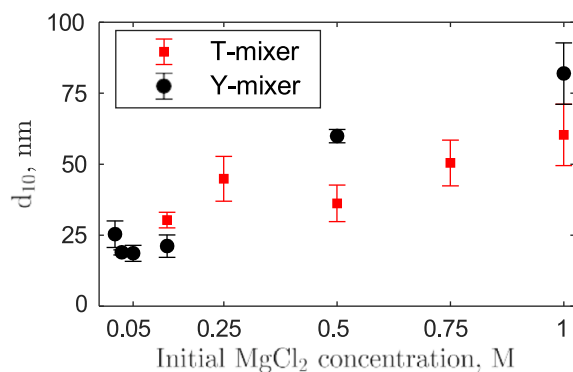
Fig. 1. Experimental values of d_{10} plotted as a function of the initial $MgCl_2$ concentration. The error bars show the standard deviation among three different experimental runs.

the final section of the mixer. Unfortunately, a similar extension was not feasible in the T-mixer, making it difficult to determine conclusively whether the reaction was completed inside the T-mixer or within the collection flask. As shown in Fig. 1, the standard deviations of particle sizes obtained in the T-mixer are, in general, larger than in the Y-mixer. Larger deviations may be due to (i) (few) crystalline bridges that do not have time to cement properly and break during ultrasonic treatment (ii) fluctuations in the measurement of the scattered light during DLS analysis, and (iii) the influence of aggregation which becomes more pronounced at higher concentrations. The increased concentration in the T-mixer may promote greater interaction and clustering of particles, leading to larger deviations in the measured particle sizes.

3. Population balance model

The mathematical model of precipitation needs to account (i) for the instantaneous, irreversible precipitation reaction, which is affected by mixing while forming the particles, and (ii) for the evolution of such particles. Due to its instantaneous nature, the modeling of the reactions and of their interaction with mixing requires consideration of certain physical quantities. Specifically, within the RANS framework, only two quantities are necessary: the mixture fraction and its variance, which can be effectively employed within the context of the beta-PDF (Probability Density Function) approach. Their evolution adequately captures the interplay between turbulent fluctuations, mixing, and extremely fast chemical reactions. The mixture fraction is a scalar quantity that describes the composition of a fluid mixture. The mixture fraction variance represents the statistical dispersion or fluctuation in the mixture fraction values within the flow; it provides information about the local degree of mixing. By tracking the evolution of the mixture fraction and its variance, one can gain insights into the mixing

characteristics and spatial distribution of different species within the flow field. In Marchisio and Fox [30], the variance ($\bar{\alpha}'^2$) was correlated to the ratio between the turbulent dissipation rate, ε, and the turbulent kinetic energy, k, according to the following equation:

$$\frac{d\left(\bar{u}\bar{\alpha}'^2\right)}{dy} = -\frac{C_\phi}{2}\frac{\varepsilon(y)}{k(y)}\bar{\alpha}'^2 \tag{4}$$

being $\bar{u}$ the fluid mean velocity, C_ϕ a fitting parameter (generally set equal to 2 within the RANS framework [30]), and y the mixing channel coordinate for the T- and Y-mixers. To obtain the k and ε profiles, CFD simulations were conducted. The methodology applied, and the obtained results are provided in the 'supporting information'. As shown in Eq. (4), the variance dissipation rate depends on a characteristic time linked to the k/ε ratio. In one of our previous publications [28], the variance profiles in the T-mixer were reported as a function of the residence time for different flow rates. A similar approach is taken in this work. The vertical coordinate is converted into a time coordinate, based on the plug flow reactor (PFR) assumption; specifically, any given spatial coordinate can be transformed into a time variable by dividing it by the mean fluid velocity. In this way, a fair comparison between the two mixers can be made using the corresponding residence times.

In Fig. 2, the mixture fraction variance evolution is shown for the T- and Y-mixers, and a characteristic time for its dissipation can be identified. One can see that in the Y-mixer, the mixing efficiency is higher than in the T-mixer. In fact, Battaglia et al. [31] empirically estimated that for the T-mixer (referring to a velocity in the mixing channel of 12.3 m/s), the characteristic mixing time was about 2 ms (using the expression provided by Schikarski et al. [19], namely Eq. (6) in their paper) which is one order of magnitude higher than that of the Y-mixer (assuming 10^{-4} s to be the time when variance becomes practically zero). The micro-mixing rate has a direct impact on the generation of supersaturation, defined as:

$$S = \frac{\gamma_\pm^3\left(\bar{c}_{Mg^{2+}}\bar{c}_{OH^-}^2\right) - k_{sp}}{k_{sp}} \tag{5}$$

where $\bar{c}_{Mg^{2+}}$ and $\bar{c}_{OH^-}$ are the concentrations calculated through the beta-PDF approach, k_{sp} is the solubility product (1.3×10^{-11}, $mol^3 l^{-3}$ - constant during the process) [32], and $\gamma_\pm$ is the solution activity coefficient. The solubility product, k_{sp}, is an equilibrium constant given by the product between the ions concentration ($k_{sp} = \bar{c}_{Mg^{2+}}\bar{c}_{OH^-}^2$) in the solution. Regarding the activity coefficient, it is important to notice that the value of $\gamma_\pm$ is not constant but calculated using Bromley's equations (for details, please refer to the 'supporting information' in our previous publication [28]). This activity coefficient varies with both the initial reactant concentrations and as the precipitation proceeds. As the initial concentration of $MgCl_2$ and $NaOH$ increases, the ionic strength of the solution also increases, leading to a decrease in the value of the activity coefficient. Furthermore, as particles nucleate, grow, and aggregate, Mg^{2+} and OH^{-1} ions migrate from the liquid to the

solid phase, reducing the ionic strength of the solution and causing the activity coefficient to increase. Both the primary nucleation rate, J, and the growth rate, G, depend on the supersaturation S, according to the following equations. The primary nucleation rate consists of two terms, which include the contribution of both homogeneous and heterogeneous nucleation:

$$J = \underbrace{A_1 e^{\left(-\frac{B_1}{\ln(S+1)^2}\right)}}_{\text{Homogeneous}} + \underbrace{A_2 e^{\left(-\frac{B_2}{\ln(S+1)^2}\right)}}_{\text{Heterogeneous}} \tag{6}$$

A_1 and A_2 represent the maximum nucleation rate when the supersaturation approaches infinity, measured in particles no. $\left(\text{m}^{-3} \text{ s}^{-1}\right)$. They determine the maximum rate at which new particles form in the system. The parameters B_1 and B_2 are dimensionless and are related to the surface tension between the liquid phase (solution) and the solid particles (e.g., $Mg(OH)_2$-liquid or foreign solid impurities-liquid). For the growth rate, the following typical power law relationship was chosen:

$$G = k_g S^g \tag{7}$$

where k_g is the rate constant for growth [m/s], while g is the dimensionless exponent for the driving force, and depends on the nature of the growth mechanism ($g = 1$ implies diffusion-controlled growth). The aggregation rate, β_{agg}, consists of a collision kernel, β_{coll}, and an aggregation efficiency, ψ [27,33]:

$$\beta_{agg} = \beta_{coll} \psi \tag{8}$$

where β_{coll} and $\psi(A_P, \varepsilon)$ can be calculated as follows:

$$\beta_{coll} = 10^{C_1} \left(\beta^{tr} + \beta^{br}\right) \tag{9}$$

$$\beta^{tr} = \sqrt{\frac{8\pi}{15}} \sqrt{\frac{\varepsilon}{\nu}} \frac{(L+\lambda)^3}{8} \tag{10}$$

$$\beta^{br} = \frac{2k_B T}{3\mu} \frac{(L+\lambda)^2}{L\lambda} \tag{11}$$

$$\psi(A_P, \varepsilon) = e^{-\frac{t_c(A_P,\varepsilon)}{t_i(\varepsilon)}} \tag{12}$$

where β^{tr} and β^{br} represent the collision frequencies due to turbulent fluctuations and Brownian motions, respectively, L and λ are the sizes of the colliding particles and k_B is the Boltzmann constant $\left(1.380649 \cdot 10^{-23} \text{ JK}^{-1}\right)$. The collision kernel (Eq. (9)) is modified by a correction factor, 10^{C_1}, in turn function of a dimensionless parameter C_1, which determines the likelihood of particles to collide. The variables t_c and t_i represent, instead, the characteristic interaction and cementation times and are defined as follows:

$$t_c = \frac{D_b}{f_s G} \tag{13}$$

$$t_i = \sqrt{\frac{\nu}{\varepsilon}} \tag{14}$$

$$D_b = \frac{L_{eq} \rho_c^{0.5} (\varepsilon \nu)^{0.25}}{A_p^{0.5}} \tag{15}$$

$$L_{eq} = \frac{L\lambda}{\left(L^2 + \lambda^2 - L\lambda\right)^{0.5}} \tag{16}$$

where ν is the kinematic viscosity of the suspending fluid (10^{-6} m^2/s), ρ_c is the crystal density (2.34 g/cm^3), f_s is a shape function [27], A_p represents the strength of the bridge formed between particles and is measured in N/m^2. Note that the difference between the aggregation kernel used here and those found in the literature [29] lies in the additional correction in Eq. (9), 10^{C_1}, which includes the fitting parameter C_1. As already mentioned, 10^{C_1}, should be regarded as a correction factor, that accounts for deviations from the ideal conditions, under which Eqs. (10)–(11) were derived (Shiea et al. [21]). It is worth mentioning that this formulation is chosen just for numerical reasons and that it is legitimate to change its values from zero (i.e., $C_1 = 0$), which corresponds to a unitary correction (i.e., $10^{C_1} = 1$), namely
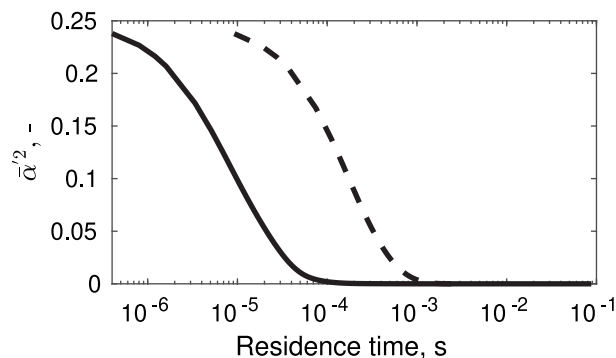

Fig. 2. Mixture fraction variance evolution as a function of the residence time for the T- and Y-mixers setups obtained solving Eq. (4). Dashed line refers to the T-mixer and solid line refers to the Y-mixer.

no correction at all. For $Mg(OH)_2$ precipitation, Raponi et al. [28] provided an expression where the C_1 parameter multiplies both contributions in Eq. (9), due to the nanometric size of the particles. The above equations set is solved in the PBM using the quadrature method of moments (QMOM) [34,35] approach:

$$\frac{d\left(\bar{u}m_j\right)}{dy} = L_c^j J + \int_0^\infty jL^{j-1} G f \, dL + \bar{B}_j - \bar{D}_j \tag{17}$$

Here, L_c is the critical size (1 nm) of a stable nucleus, whereas $\bar{B}_j$ and $\bar{D}_j$ model the birth and the death term linked to a net aggregation rate. In the present work, 3 quadrature nodes (or, consequently, 6 moments) were used. Ultimately, the PBM is closed by resorting to a mass balance for ions that, upon reacting, disappear from the liquid phase to form the solid:

$$\frac{d\left[Mg^{2+}\right]}{dy} = -\frac{\rho_c k_v}{M_c} \frac{dm_3}{dy} \tag{18}$$

$$\frac{d\left[OH^-\right]}{dy} = -2\frac{\rho_c k_v}{M_c} \frac{dm_3}{dy} \tag{19}$$

Here, ρ_c, and M_c are the density and molecular weight of the solid $\left(2.34 \text{ g/cm}^3 \text{ and } 58.32 \text{ g/mol}\right)$ respectively and k_v is the shape factor ($\pi/6$ for spheres). The PBM is implemented in MatLab and the equations system (namely, Eqs. (17), (18), (19)) is solved using 'ode15s' algorithm. There are a total of eight model parameters to estimate: four stemming from the nucleation rate equation J (A_1, A_2, B_1, B_2), two from the growth rate equation G (k_g, g), and two, C_1 and A_p, from the aggregation rate equation. The estimation of these model parameters is crucial for accurately representing particle dynamics. In our previous study [28], the optimization of these model parameters was extensively discussed. A brief explanation of the parameter estimation is also provided in the 'supporting information' of this paper for completeness.

4. Results and discussion

The parameters set (8 parameters) was estimated by comparing the simulation results with the experimental data (20 data points) collected using the T-mixer. Then, such a parameter set was validated against the experimental data obtained in the Y-mixer. The parameters and their physical interpretation are discussed in the following.

T-mixer parameter identification. The kinetic parameters listed in Table 2 have specific physical meanings, reflecting the relative importance of the corresponding phenomena involved in the process.

Examining the different rates makes it possible to further assess whether the obtained parameters are physically realistic, as well as the estimation of the confidence interval (see 'supporting information'). These kinetic parameters play a crucial role in determining the change in the total particle number (zeroth-order moment).

Table 2
Kinetic parameters set.

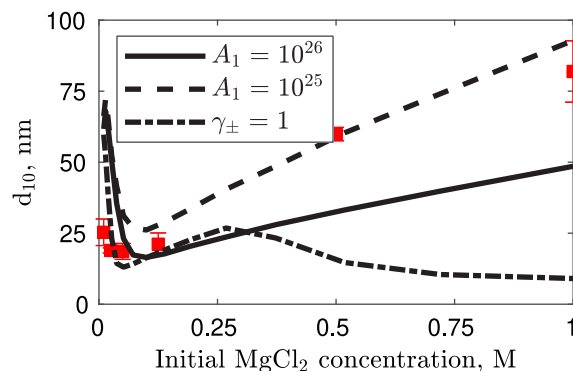| Parameter	A_1	A_2	B_1	B_2	k_g	g	C_1	A_p
Set #1	10^{26}	10^{14}	301	30	10^{-10}	1	0.86	5.9
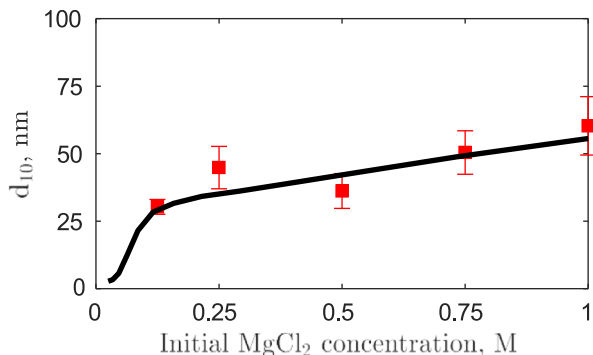
Fig. 3. Experimental data (d_{10}) collected using the T-mixer for different initial concentrations of $MgCl_2$ (red squares). The inferred parameters are used to fit the data and extrapolate the sizes trend for lower initial $MgCl_2$ concentrations (black solid line).

Fig. 4. Experimental data (d_{10}) collected using the Y-mixer for different initial concentrations of $MgCl_2$ (red squares). Simulation results are shown with three black curves. PBM without modification (solid line), PBM with modified $A_1 = 10^{26}$ particle no $(m^{-3}s^{-1})$ (dashed lined), PBM with constant $\gamma_{\pm} = 1$ (dash-dotted line).

In Fig. 3, the calculated values of d_{10} (black solid line) are plotted together with the experimental data (red squares) obtained in the T-mixer, thus showing quite a good agreement between the two. It is worth noting that the simulations were extended to include initial $MgCl_2$ concentration levels lower than in the experiments, showing that the particle size decreases when the concentration is decreased. In conclusion, the overall trend of d_{10} is that it increases monotonically with the initial $MgCl_2$ concentration.

Y-mixer model validation. We utilized the parameters obtained from the T-mixer to predict the values of d_{10} for the $Mg(OH)_2$ particles obtained in the Y-mixer. While the structure of the PBM remained identical, it was essential to consider the significant differences in flow dynamics and turbulent fields between the two mixers (see 'supporting information'). We incorporated the k and ε profiles obtained through CFD simulations specific for the Y-mixer to account for these variations.

In Fig. 4, the dependence of d_{10} on the initial concentration of $MgCl_2$ is shown for the case of the Y-mixer. The experimental data, red boxes, are plotted together with three curves calculated by using the model. The first curve (solid line) corresponds to the trend predicted by the model keeping the same set of kinetic parameters obtained for the T-mixer, while considering the fluid dynamics characterizing the new Y-mixer system. The second curve (dashed line) represents the trend that would occur if the parameter A_1 were reduced by one order of magnitude. The third curve (dash-dotted line) shows the behavior that would be observed if the activity coefficient had a value of one regardless of the operating conditions.

By comparing the experimental measurements with the model results, we can assess the sensitivity of the model to different parameters. When utilizing the same parameters estimated from the T-mixer and, when the specific turbulent profiles obtained through CFD simulations for the Y-mixer are employed, the overall experimental trend is captured, including the occurrence of the minimum. However, there is a slight underestimation and a slight overestimation of d_{10} at high and at low values of the initial $MgCl_2$ concentration, respectively. Adjusting the value of A_1 to be one order of magnitude lower yields the same qualitative trend, while improving the agreement at high initial $MgCl_2$ concentrations. Although this adjustment may seem large, A_1 represents, by definition, the homogeneous nucleation rate when the supersaturation approaches infinity. At lower supersaturation, the primary nucleation rate decreases below A_1 until the heterogeneous nucleation becomes larger and takes over. Fine-tuning the A_1 value

allows the model not only to predict the overall trend but also to match the experimental data accurately. While the other parameters also influence the predictions, the primary nucleation rate, proportional to A_1, has the most significant impact, thus proving the key role played by A_1. Moreover, Fig. 4 (dash-dotted line) highlights the importance of incorporating the solution non-ideality [36,37]; while assuming ideality in the PBM would still yield reasonably accurate predictions for highly diluted solutions, it would lead to a significant underestimation of d_{10} for concentrated ones.

Modeling insights. After proving its accuracy, we can utilize the model to better understand the underlying phenomena. Particular attention will be paid to the minimum in d_{10} when varying the initial $MgCl_2$ concentration, experimentally observed in the Y-mixer (Fig. 4). To this aim, the evolution of the relevant properties of the systems as a function of the residence time will be analyzed in detail for three concentrations: one on the left of the minimum (i.e., 0.025 M), one at the minimum (i.e., 0.1 M, as obtained through simulations) and one on its right (i.e., 1 M). The zeroth-order moment, m_0, was chosen among all physical quantities to explain the phenomena observed. Indeed, if only molecular processes (i.e., nucleation and growth) are considered, the zeroth-order moment exhibits a sigmoidal shape: it starts from zero (for non-seeded systems) and reaches the upper asymptotic value due to nucleation (growth does not change m_0). Therefore, the zeroth-order moment reaches a plateau for a system where aggregation does not occur. When aggregation is considered, as soon as particles collide and stick together, the zeroth-order moment decreases. Let us first examine the observations from the T-mixer configuration. Fig. 5-*left* reports the evolution of the zeroth-order moment along the mixing channel, i.e., in terms of residence time; it showcases the combined impact of nucleation, growth, and aggregation for the T-mixer. The final residence time in the T-mixer corresponds to the duration required for the fluid to flow through the mixing channel, which, as mentioned, could not be adequately extended. The results obtained from the T-mixer reveal a distinct trend. As depicted in Fig. 5-*right*, supersaturation gradually builds up, triggering nucleation and subsequent particle growth. Consequently, the zeroth-order moment (m_0) initially exhibits an upward trend, due to the formation of particles. However, particle aggregation eventually decreases the value of m_0. Notably, lower initial $MgCl_2$ concentrations result in lower maximum supersaturation levels, thereby delaying nucleation's inception and leading to fewer particles. Next, let us consider the Y-mixer configuration. The final coil length in the Y-mixer (hence the residence time) was varied based on the concentrations employed in the corresponding experiments (Table 1), as elucidated in Section 2. Specifically, to ensure completion of the reaction as the concentration range was extended towards smaller concentrations, the final coil length in the Y-mixer was increased
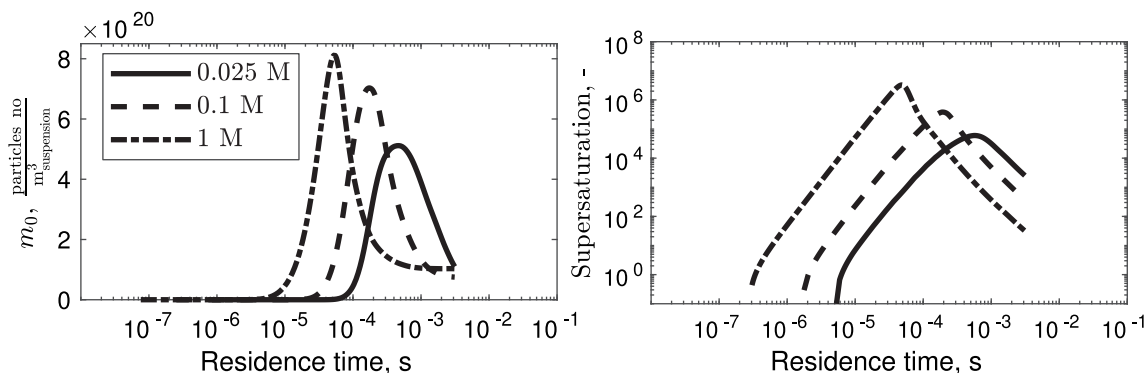
Fig. 5. m_0 (*left*) and supersaturation (*right*) profiles plotted as a function of the T-mixer residence time for three different initial $MgCl_2$ concentrations.
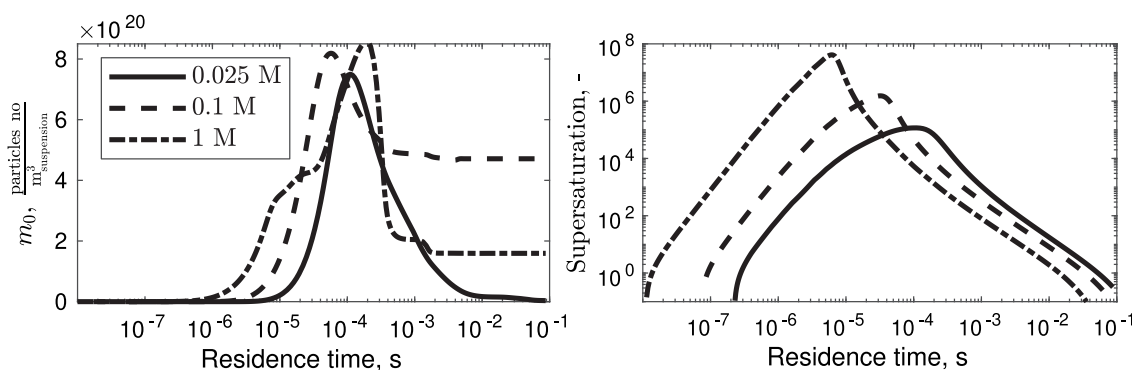

Fig. 6. m_0 (*left*) and supersaturation (*right*) profiles plotted as a function of the Y-mixer residence time for three different initial $MgCl_2$ concentrations.

accordingly (see 'supporting information'). In Fig. 6, the reported residence time corresponds to the duration required to achieve complete conversion of the reactants in the least concentrated solution, although the total simulation time is always equal to the residence time at a given operating condition (see Table 1). It is worth noticing that this residence time suffices for all other cases, as the driving force amplifies with an increase in the initial $MgCl_2$ concentration. For the Y-mixer (Fig. 6-*left*), a distinct monotonic trend similar to that observed in the T-mixer configuration is not evident, even though the supersaturation profiles for both setups (Fig. 5-*right* and Fig. 6-*right*) exhibit similar trends. One plausible explanation for this trend in the Y-mixer is based on the selectivity of supersaturation. In our investigation, we have explored how the depletion of supersaturation occurs as a direct result of changing the concentration of $MgCl_2$. It is worth recognizing that the dominant mechanism by which supersaturation is depleted varies for different operating conditions. This is further elaborated with the help of Fig. 7, which shows the relationship between the nucleation rate (J) and the molecular growth rate (G) at different levels of supersaturation.

In Fig. 7 J is plotted against G for increasing supersaturation levels. Due to the highly non-linear nucleation rate the plot is divided into two parts: on the left J is plotted versus G for lower supersaturation levels, whereas on the right the same quantities are plotted for higher supersaturation levels. It is important to notice that Fig. 7 is based on the kinetics of the specific compound under study (Eqs. (6) and (7)). Three distinct regions can be observed: (i) a metastable region where the nucleation rate variation with the growth rate (dJ/dG) is almost zero, (ii) a second region where $dJ/dG \to \infty$ (indicating a significant increase in the nucleation rate), and (iii) a third region exhibiting a similar trend of the metastable one but at much higher rates (as supersaturation approaches infinity). This behavior, observed in both crystallization and precipitation processes, was explained by Kubota and co-workers [38,39] and supports the concept of supersaturation selectivity. Particle growth is favored over nucleation in the metastable region (i). Understanding this concept helps explain the behavior in

region (iii), where the nucleation rate is hindered by the growth of existing particles, resulting in fewer particles that grow larger. Conversely, in region (ii), the nucleation rate increases significantly, depleting supersaturation to form more particles that grow slower. It is worth noticing that the metastable region (i) is hardly accessible in precipitation processes, due to the high supersaturation levels generated even at low concentrations. Therefore, considering regions (ii) and (iii) allows for a better explanation of the trends observed in m_0 at different concentrations (Fig. 6 *left*) and it helps explain the presence of the minimum in the d_{10} trend (Fig. 1). To assess the influence of each phenomenon, we numerically decoupled molecular processes and secondary processes. We begin by considering a hypothetical scenario where only molecular processes are enabled, and only subsequently, the contribution of aggregation is introduced.

The *left* panel of Fig. 8 focuses on the m_0 evolution for three concentrations as a function of the residence time when solely molecular processes are considered. The *right* panel of Fig. 8, instead, shows three trends of the d_{10} as a function of the initial concentration of $MgCl_2$. The blue line represents the d_{10} trend when all processes are accounted for. The green line represents the d_{10} trend when nucleation, growth, and Brownian aggregation are considered. Lastly, the red line represents the d_{10} trend when only nucleation and growth processes are considered. For the sake of clarity, let us call 'primary particles' the particles that would potentially occur if aggregation could be prevented (red line), while 'particles' are those that actually result considering aggregation as well (green and blue lines). Moreover, it is worth noticing that molecular and secondary processes do not occur in series but in parallel. Therefore, decoupling the phenomena is merely a numerical expedient through which the discussion can be facilitated. It is evident from the *right* panel that when only nucleation and growth are considered (Fig. 8-*right*, red line), the d_{10} exhibits a monotonically increasing trend with increasing initial $MgCl_2$ concentration. This observation is consistent with the findings presented in Fig. 7. Specifically, as the concentration increases, the system moves towards the region
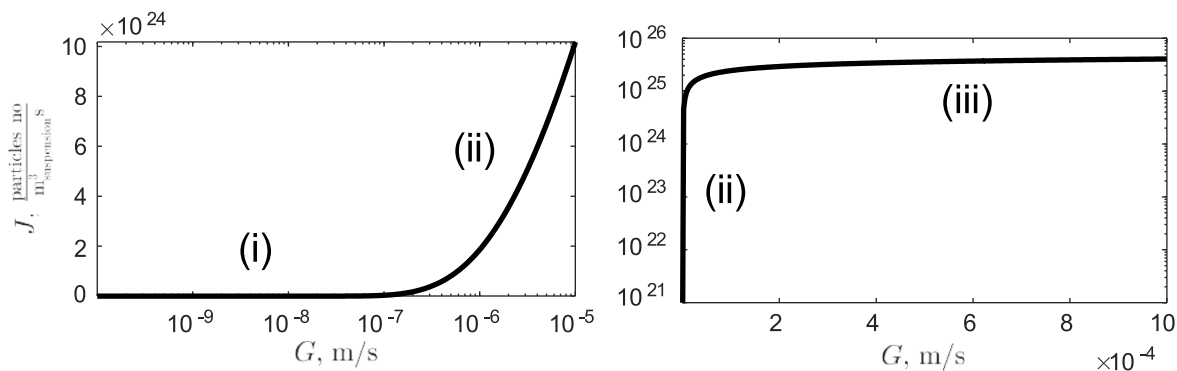
Fig. 7. Primary nucleation rate as a function of the molecular growth rate for Mg(OH)$_2$. Three regions are identified: (i) the metastable region (S from 0 to $\sim 10^3$), (ii) a nucleation-dominant region (S from $\sim 10^3$ to $\sim 10^5$), and (iii) a growth-dominant region at higher supersaturation levels (S from $\sim 10^5$ onward).
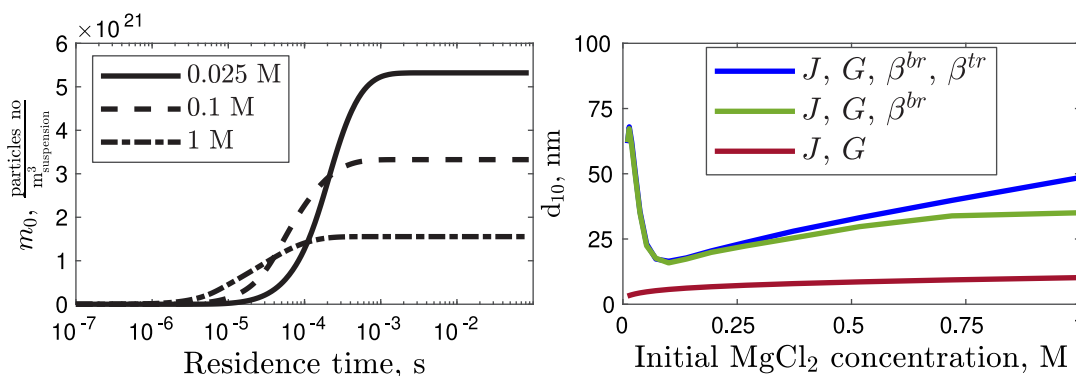

Fig. 8. m_0 evolution in the Y-mixer considering only molecular processes (*left*); d$_{10}$ trends as a function of the initial MgCl$_2$ concentration (*right*).

(iii), indicating that growth is favored over nucleation. Hence, the number of 'primary particles' decreases (Fig. 8-*left*), implying that the collision frequency decreases and so does the 'particles' size. As it can be seen by comparing the blue and green lines in Fig. 8-*right*, the Brownian contribution alone in Eq. (8) produces the minimum, due to the interplay between the collision frequency, β_{coll}, and the aggregation efficiency, ψ, (Eq. (8)). Indeed, as the concentration increases, the cementation time (Eq. (13)) decreases since it is inversely proportional to G. The interaction time (Eq. (14)) is constant since the flow rate is the same (and consequently so are the flow field and the turbulence fields). A decrease in the cementation time, for the same interaction time, results, on average, in an increase in the aggregation efficiency. Therefore, the minimum observed in Fig. 4 for the Y-mixer is a consequence of the opposite trends of the collision frequency and aggregation efficiency with the initial MgCl$_2$ concentration. It is worth noting that the aggregation efficiency (Eq. (12)) depends on fluid dynamics, local supersaturation, and particle sizes and, due to the highly intricate dependencies among these factors, a detailed analysis cannot be performed independently (see 'supporting information'). Moreover, the contribution of turbulent aggregation to d$_{10}$ is negligible except for high initial MgCl$_2$ concentrations, as depicted in (Fig. 6-*right*) by comparing the blue and green lines. This could be due to the faster desupersaturation process, resulting in a broader particle size distribution where the bigger 'particles' undergo turbulent aggregation, resulting in an increase of d$_{10}$.

Improvements in the aggregation kernel. Let us now investigate the role of the correction factor, 10^{C_1}, contained in Eq. (9).

As mentioned this correction accounts for deviations from the simplification hypotheses under which the aggregation kernels are derived, notably a sufficiently low total particle concentration. By using an empirical approach it is therefore reasonable to link this correction to

the total mass of the precipitated solid, proportional to the third-order moment of the PSD:

$$10^{C_1} = 10^{C_1' m_3(t)} \tag{20}$$

The third-order moment, m_3, is calculated accounting for the increasing mass of the precipitated solid. This modification enables us to track the history of solid generation throughout the process at each operating condition. At the beginning of the precipitation process, there is minimal precipitated solid $(m_3 \to 0)$ and $10^{C_1' m_3 \to 0}$ approximates 1. As the precipitation process unfolds, the amount of the precipitated solid increases, and consequently, m_3 rises, leading to an increase in $10^{C_1' m_3}$. Additionally, while m_3 starts at zero for all operating conditions, its final value significantly differs with varying initial concentrations of the reactants. This means that $10^{C_1' m_3}$ not only increases with the precipitation process advance but also scales proportionally with the initial concentration of the reactants introduced into the reactor, implying a heightened contribution from aggregation. This modification thus reinforces the already existing correlation between the number of particles and the collision frequency for which the collision frequency increases as the number of particles increases. The choice of the third-order moment is deliberate, as it remains independent of the aggregation source term itself. It is noteworthy that this change in the kernel does not increase the number of parameters.

A new parameter identification was therefore conducted on this modified model by using the T-mixer experimental data (Fig. 9 *left*), with subsequent validation and comparison of simulation predictions against experiments conducted on the Y-mixer (Fig. 9 *right*). One can see that the experimental T-mixer trend is better represented because the model can assure a change in the second derivative (i.e., initially concave and then convex) for the d$_{10}$ as a function of the initial reactant concentration instead of a linear trend. The enhanced predictive capabilities of the model are evident also for the Y-mixer configuration.
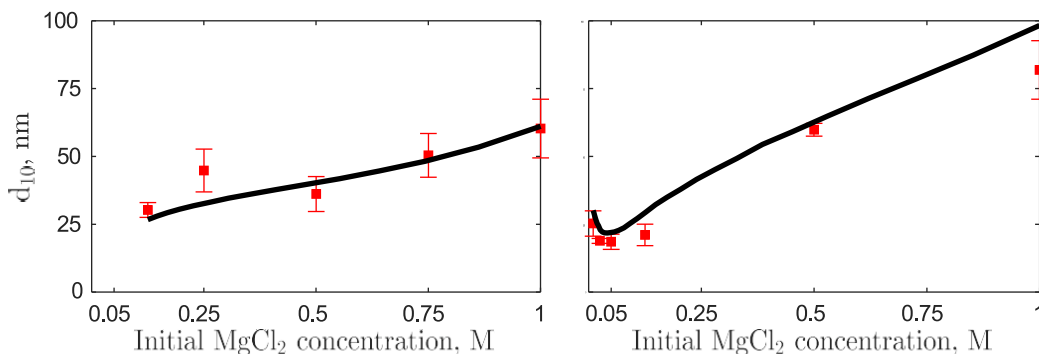
Fig. 9. Numerical simulations run for the T-(*left*) and Y-(*right*) mixer accounting for the new correction factor shown in Eq. (20). The numerical results (solid line) are plotted together with the experimental data (red squares).
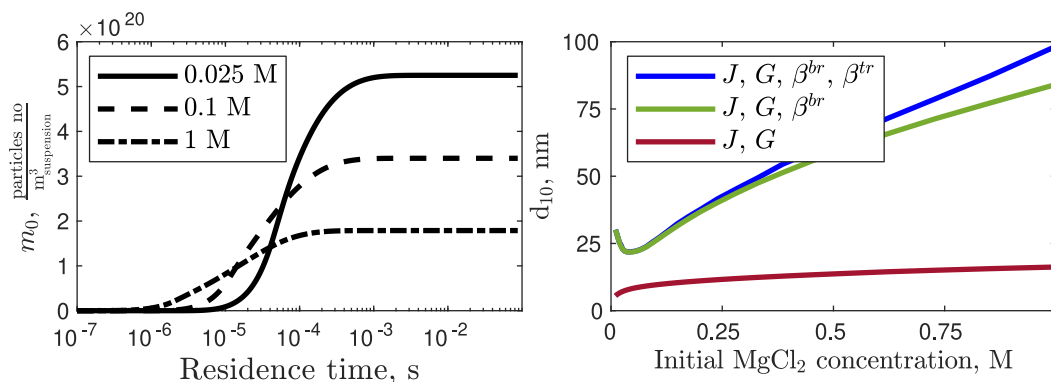

Fig. 10. m_0 evolution in the Y-mixer considering only molecular processes (*left*); d_{10} trends as a function of the initial $MgCl_2$ concentration (*right*). Simulations are run using Eq. (20).

Table 3
Model parameters for aggregation kernel as a function of m_3 (#2).

Parameter	A_1	A_2	B_1	B_2	k_g	g	C_1'	A_p
Set #2	$10^{25.8}$	$10^{13.9}$	301	34	$10^{-10.4}$	1.45	29.39	6.37

It should also be noticed in Fig. 10 that the introduction of this new correction factor only affects the accuracy of the predictions but not the interaction between the various processes. The comparison between Fig. 8 and Fig. 10 shows that the trend of m_0 and d_{10} remains unchanged qualitatively but changes quantitatively. It follows that the model is able to adequately describe the (intricate) interaction of the phenomena involved and that the introduction of the new correction factor better approximates the particle collision mechanism.

The parameters set found through this second optimization is reported in Table 3 and can be compared with the initial parameters set (see 'supporting information' for further details on confidence interval estimation). As it is seen most of the identified parameters do not change significantly and only the correction factor is tuned accordingly.

To summarize, using the new functional form for the correction factor multiplying the aggregation rate, as expressed by Eq. (20), leads to a significant improvement in the numerical predictions for both the T-mixer and the Y-mixer. Indeed, set #2 is able to describe both datasets (Fig. 9) simply by considering the change of fluid dynamics from the T- to the Y-mixer without further change.

5. Conclusions

This work focuses on the numerical predictions of $Mg(OH)_2$ precipitation when quite different systems (T- and Y-mixer) are involved. A mono-dimensional model was used to model the $Mg(OH)_2$ precipitation in both T- and Y-mixers. Using an identical set of kinetic parameters, we carefully considered the different fluid dynamics and turbulence features that characterized the two configurations by conducting CFD simulations. The numerical framework demonstrated its capability to accurately predict and describe the precipitation phenomena when transitioning from a T- to a Y-mixer. The model was tuned for a T-mixer system and its prediction capability was assessed when a Y-mixer with two divergent channels and a final coil system was used, by only numerically accounting for the new hydrodynamics with no further adjustments. Furthermore, we provided a comprehensive physical interpretation of the dominant phenomena governing the precipitation process. Finally, a novel semi-empirical correction factor based on the third-order moment of the particle size distribution, m_3, was proposed for the aggregation rate. This last correction factor has provided the best quantitative trend compared with the experimental values. It is worth underlining that the ultimate purpose of this novel predictive model (and framework), which has been tuned and validated in this work, will be used for the design of a crystallizer prototype aimed at controlling the granulometry of Magnesium Hydroxide precipitates [40].

CRediT authorship contribution statement

Antonello Raponi: Conceptualization, Methodology, Software, Validation, Formal analysis, Investigation, Data curation, Writing – original draft, Writing – review & editing, Visualization. **Ramona Achermann:** Conceptualization, Methodology, Validation, Formal analysis, Data curation, Writing – review & editing, Visualization. **Salvatore Romano:** Conceptualization, Methodology, Validation, Writing – review & editing. **Silvio Trespi:** Conceptualization, Methodology, Validation, Writing – review & editing, Visualization. **Marco Mazzotti:**

Conceptualization, Methodology, Resources, Writing – review & editing, Visualization, Supervision, Project administration, Funding acquisition. **Andrea Cipollina:** Conceptualization, Methodology, Visualization, Writing – review & editing, Project administration, Funding acquisition. **Antonio Buffo:** Conceptualization, Methodology, Supervision. **Marco Vanni:** Conceptualization, Methodology, Supervision. **Daniele Marchisio:** Conceptualization, Methodology, Writing – review & editing, Visualization, Supervision, Project administration, Funding acquisition.

Declaration of competing interest

The authors declare that they have no known competing financial interests or personal relationships that could have appeared to influence the work reported in this paper.

Data availability

Data will be made available on request.

Acknowledgments

Appendix A. Supplementary data

Supplementary material related to this article can be found online at https://doi.org/10.1016/j.cej.2023.146540. This material includes further details on CFD-PBM coupling, parametric identification and aggregation kernel.

References

[1] C.M. Tai, R.K. Li, Studies on the impact fracture behaviour of flame retardant polymeric material, Mater. Des. 22 (2001) 15–19.

[2] H. Béarat, M.J. McKelvy, A.V. Chizmeshya, R. Sharma, R.W. Carpenter, Magnesium hydroxide dehydroxylation/carbonation reaction processes: Implications for carbon dioxide mineral sequestration, J. Am. Ceram. Soc. 85 (2002) 742–748.

[3] X. Chen, J. Yu, S. Guo, Structure and properties of polypropylene composites filled with magnesium hydroxide, J. Appl. Polym. Sci. 102 (2006) 4943–4951.

[4] S. Zhang, F. Cheng, Z. Tao, F. Gao, J. Chen, Removal of nickel ions from wastewater by Mg(OH)2/MgO nanostructures embedded in Al2O3 membranes, J. Alloys Compd. 426 (2006) 281–285.

[5] H. Gui, X. Zhang, W. Dong, Q. Wang, J. Gao, Z. Song, J. Lai, Y. Liu, F. Huang, J. Qiao, Flame retardant synergism of rubber and Mg(OH)2 in EVA composites, Polymer 48 (2007) 2537–2541.

[6] S. Kakaraniya, C. Kari, R. Verma, A. Mehra, Gas absorption in slurries of fine particles: So2 - Mg(OH) 2 - MgSO3 system, Ind. Eng. Chem. Res. 46 (2007) 1904–1913.

[7] H. Cao, H. Zheng, J. Yin, Y. Lu, S. Wu, X. Wu, B. Li, Mg(OH)2 complex nanostructures with superhydrophobicity and flame retardant effects, J. Phys. Chem. C. 114 (2010) 17362–17368.

[8] A. Sierra-Fernandez, L.S. Gomez-Villalba, O. Milosevic, R. Fort, M.E. Rabanal, Synthesis and morpho-structural characterization of nanostructured magnesium hydroxide obtained by a hydrothermal method, Ceram. Int. 40 (8 PART A) (2014) 12285–12292.

[9] C.M.F. dos Santos, A.F.B. Andrade, S.D.F. Rocha, S.D.J.O.A. Journals, The effect of caustic magnesia natural impurities on magnesium oxide hydroxylation, 2017.

[10] X. Song, K. Tong, S. Sun, Z. Sun, J. Yu, Preparation and crystallization kinetics of micron-sized Mg(OH)2 in a mixed suspension mixed product removal crystallizer, Front. Chem. Sci. Eng. 7 (2013) 130–138.

[11] J.W. Mullin, Crystallization, Elsevier, 2001.

[12] A. Mersmann, Crystallization Technology Handbook, Marcel Dekker, 2001, p. 832.

[13] J. Baldyga, W. Podgorska, R. Pohorecki, Mixing-precipitation model with application to double feed semibatch precipitation, Chem. Eng. Sci. 50 (1995) 1281–1300.

[14] D.L. Marchisio, R.O. Fox, A.A. Barresi, G. Baldi, On the comparison between presumed and full PDF methods for turbulent precipitation, Ind. Eng. Chem. Res. 40 (2001) 5132–5139.

[15] D.L. Marchisio, A.A. Barresi, M. Garbero, Nucleation, growth, and agglomeration in barium sulfate turbulent precipitation, AIChE J. 48 (2002) 2039–2050.

[16] D.L. Marchisio, A.A. Barresi, CFD simulation of mixing and reaction: The relevance of the micro- mixing model, Chem. Eng. Sci. 58 (2003) 3579–3587.

[17] P.V. Danckwerts, The effect of incomplete mixing on homogeneous reactions, Chem. Eng. Sci. 8 (1958) 93–102.

[18] G.W. Becker, M.A. Larson, Mixing effects in continuous crystallization, in: J.A. Palermo, M.A. Larson (Eds.), Crystallization from Solutions and Melts, Springer US, Boston, MA, 1969, pp. 14–23.

[19] T. Schikarski, H. Trzenschiok, W. Peukert, M. Avila, Inflow boundary conditions determine T-mixer efficiency, React. Chem. Eng. 4 (2019) 559–568.

[20] T. Schikarski, M. Avila, H. Trzenschiok, A. Güldenpfennig, W. Peukert, Quantitative modeling of precipitation processes, J. Chem. Eng. 444 (2022) 136195.

[21] M. Shiea, A. Querio, A. Buffo, G. Boccardo, D. Marchisio, CFD-PBE modelling of continuous Ni-Mn-Co hydroxide co-precipitation for Li-ion batteries, Chem. Eng. Res. Des. 177 (2022) 461–472.

[22] R.O. Fox, On the relationship between Lagrangian micromixing models and computational fluid dynamics 1, Chem. Eng. Process. 37 (1998) 521–535.

[23] L. Bosetti, M. Mazzotti, Study of secondary nucleation by attrition of potassium alum crystals suspended in different solvents, Cryst. Growth Des. 20 (4) (2020) 2570–2577.

[24] J. Bałdyga, W. Orciuch, Some hydrodynamic aspects of precipitation, Powder Technol. 121 (2001) 9–19.

[25] L. Wang, D.L. Marchisio, R.D. Vigil, R.O. Fox, CFD simulation of aggregation and breakage processes in laminar Taylor-Couette flow, J. Colloid Interface Sci. 282 (2005) 380–396.

[26] E. Gavi, D.L. Marchisio, A.A. Barresi, M.G. Olsen, R.O. Fox, Turbulent precipitation in micromixers: CFD simulation and flow field validation, Chem. Eng. Res. Des. 88 (2010) 1182–1193.

[27] R. David, P. Marchal, J.P. Klein, J. Villermaux, Crystallization and precipitation engineering-III. A discrete formulation of the agglomeration rate of crystals in a crystallization process, Chem. Eng. Sci. 46 (1991) 205–213.

[28] A. Raponi, S. Romano, G. Battaglia, A. Buffo, M. Vanni, A. Cipollina, D. Marchisio, Computational modeling of magnesium hydroxide precipitation and kinetics parameters identification, Cryst. Growth Des. 23 (7) (2023) 4748–4759.

[29] P.M. Orlewski, M. Mazzotti, Modeling of mixing-precipitation processes: Agglomeration, Chem. Eng. Technol. 43 (6) (2020) 1029–1039.

[30] D. Marchisio, R. Fox, Reacting flows and the interaction between turbulence and chemistry, in: Reference Module in Chemistry, Molecular Sciences and Chemical Engineering, 2016.

[31] G. Battaglia, S. Romano, A. Raponi, D. Marchisio, M. Ciofalo, A. Tamburini, A. Cipollina, G. Micale, Analysis of particles size distributions in Mg(OH)2 precipitation from highly concentrated MgCl2 solutions, Powder Technol. 398 (2022) 117106.

[32] O. Söhnel, Electrolyte crystal-aqueous solution interfacial tensions from crystallization data, J. Cryst. Growth 57 (1982) 101–108.

[33] G. Wilemski, On the derivation of Smoluchowski equations with corrections in the classical theory of Brownian motion, J. Stat. Phys. 14 (1976) 153–169.

[34] D.L. Marchisio, J.T. Pikturna, R.O. Fox, R.D. Vigil, A.A. Barresi, Quadrature method of moments for population-balance equations, AIChE J. 49 (2003) 1266–1276.

[35] D.L. Marchisio, R.D. Vigil, R.O. Fox, Quadrature method of moments for aggregation-breakage processes, J. Colloid Interface Sci. 258 (2003) 322–334.

[36] L.A. Bromley, Thermodynamic properties of strong electrolytes in aqueous solutions, AIChE J. 19 (1973) 313–320.

[37] E. Rodil, J.H. Vera, Individual activity coefficients of chloride ions in aqueous solutions of MgCl 2 , CaCl 2 and BaCl 2 at 298.2 K, Fluid Ph. Equilibria (2001) 15–27.

[38] N. Kubota, N. Doki, M. Yokota, A. Sato, Seeding policy in batch cooling crystallization, Powder Technol. 121 (1) (2001) 31–38.

[39] H.Y. Wang, J.D. Ward, Seeding and optimization of batch reactive crystallization, Ind. Eng. Chem. Res. 54 (2015) 9360–9368.

[40] C. Morgante, F. Vassallo, G. Battaglia, A. Cipollina, F. Vicari, A. Tamburini, G. Micale, Influence of operational strategies for the recovery of magnesium hydroxide from brines at a pilot scale, Ind. Eng. Chem. Res. 61 (41) (2022) 15355–15368.